Substrate-Integrated Hybrid Metallo-Dielectric Waveguide Architecture for Millimeter-Wave and Terahertz Applications

Chun-Mei Liu, *Graduate Student Member, IEEE*, Louis-Philippe Carignan, *Member, IEEE*, Shaoqiu Xiao, *Member, IEEE*, Yejun He, *Senior Member, IEEE*, and Ke Wu, *Fellow, IEEE*

***Abstract*— In millimeter-wave (mmW) and terahertz (THz) applications, the transmission behavior along circuit structures and components, such as radiation and leakage losses, is critical for their overall performances. It is imperative to develop low-loss interconnect and transmission techniques that should be used for the construction of building circuit blocks and elements. In this work, a hybrid metallo-dielectric (MD) waveguide architecture is proposed and studied for the first time. The scheme is made of mixed substrate-integrated dielectric waveguide (SIDW) and substrate-integrated nonradiative dielectric (SINRD) waveguide, which are deployed for the design of specific building parts in consideration of respective transmission properties of the two waveguides. A back-to-back WR3-band prototype based on this hybrid scheme is investigated theoretically and validated experimentally. The hybrid MD waveguide architecture with SINRD is found to outperform the hybrid MD waveguide architecture with substrate-integrated waveguide (SIW) in terms of transmission performance and manufacturing complexity because of the advantageous features of metallized-via-free structure. The presented hybrid MD waveguide architecture shows its potential for developing low-loss highly integrated mmW and THz circuits and systems.**

***Index Terms*— Hybrid metallo-dielectric (MD) waveguide, millimeter wave (mmW), substrate-integrated dielectric waveguide (SIDW), substrate-integrated nonradiative dielectric (SINRD) waveguide, terahertz (THz).**

I. Introduction

DIELECTRIC waveguide (DW) has been well known for its great potential for the development of RF/wireless communications and sensing systems due to its attractive loss properties free from conductors when operating over millimeter-wave (mmW) and terahertz (THz) bands [1]. Solid-core DW structures [2], [3], [4], [5], [6], [7], which demand for a simpler manufacturing process, are good candidates for integrated circuits and systems. Ultralow-loss transmission can basically be achieved by deploying low-loss dielectric materials. Furthermore, the overall transmission loss can be reduced by optimizing the geometry and dimension of a DW cross-sectional profile. In [8], [9], and [10], a dielectric ribbon waveguide with polymer coating was developed. In [11], substrate-integrated DW (SIDW) was studied and characterized, which resembles substrate-integrated image guide (SIIG) [12] without a metallic grounding. The SIDW geometry is self-supported by its bilateral air-hole perforated region. The SIDW is still subject to a potential leakage such as other DW structures, which stems from any transmission discontinuities due to its open geometric nature.

In understanding the detrimental nature of waveguide discontinuities, one may adopt smoothing transmission topologies, which is one straightforward way to reduce the effects of discontinuities, thus mitigating inherent radiation leakage losses. When space is limited, smooth transitions or discontinuities are impractical. Shielded waveguides, such as substrate-integrated waveguide (SIW), can be used jointly with discontinuities. Such a hybrid architecture, schematically shown in Fig. 1(a), can yield a compact structure. Metallized via fences can suppress some undesired modes and improve the transmission performance, but at the expense of increased topological complexity and metallic loss. On the other hand, a DW surrounded by a lower permittivity cladding is known to suffer less loss in the bend region [13].

Nonradiative dielectric (NRD) waveguide [14], [15], [16], [17] provides an alternative solution for the above-described leakage problem in connection with DW geometries. More recently, a substrate-integrated NRD (SINRD) waveguide based on a synthesis of the original nonplanar topology in planar form emerges as an interesting alternative [18], [19], [20], [21], which can be realized by using a planar circuit board (PCB) technology and other planar processing techniques. The SINRD waveguide is promising for mmW and THz integrated systems due to its high tolerance and resilience to sharp discontinuities as well as its resulting planar geometric structure.

Manuscript received 22 December 2022; revised 8 February 2023; accepted 17 February 2023. Date of publication 6 March 2023; date of current version 5 September 2023. This work was supported in part by the National Science and Engineering Research Council (NSERC) of Canada through the Discovery Grant Program. *(Corresponding author: Chun-Mei Liu.)*

Chun-Mei Liu, Louis-Philippe Carignan, and Ke Wu are with the Poly-Grames Research Center, Department of Electronic Engineering, Polytechnique Montréal, Montreal, QC H3T 1J4, Canada (e-mail: chunmei.liu@polymtl.ca; louis-philippe.carignan@polymtl.ca; ke.wu@polymtl.ca).

Shaoqiu Xiao is with the School of Electronics and Information Technology, Sun Yat-sen University, Guangzhou 510275, China (e-mail: xiaoshq8@mail.sysu.edu.cn).

Yejun He is with the State Key Laboratory of Radio Frequency Heterogeneous Integration, College of Electronics and Information Engineering, Shenzhen University, Shenzhen 518060, China (e-mail: heyejun@126.com).

Color versions of one or more figures in this article are available at https://doi.org/10.1109/TMTT.2023.3249047.

Digital Object Identifier 10.1109/TMTT.2023.3249047

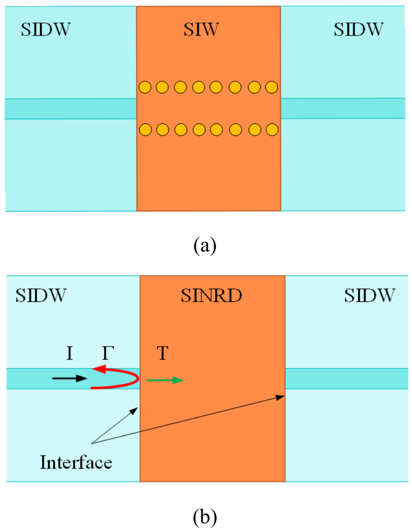

Fig. 1. (a) Existing hybrid waveguide architecture consisting of SIDW and SIW. (b) Scheme of the proposed hybrid waveguide architecture consisting SIDW and SINRD waveguide.

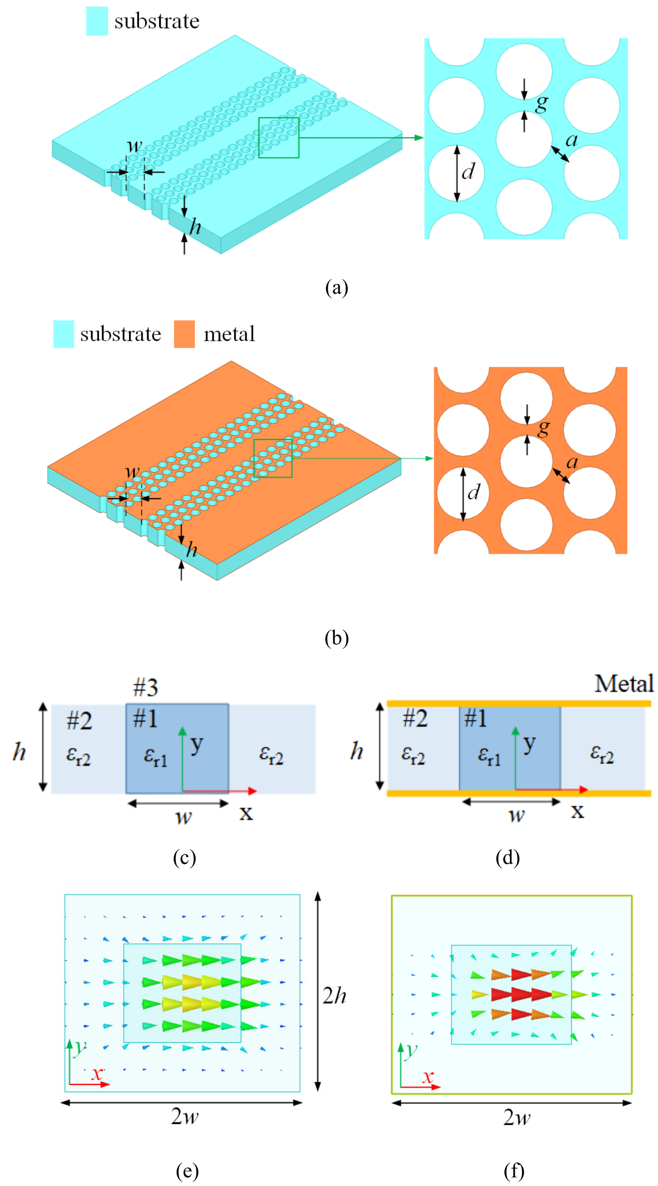

Fig. 2. Structures of (a) SIDW and (b) SINRD waveguide. Equivalent models of (c) SIDW and (d) SINRD waveguide. Simulated transverse electric field patterns of (e) E^x_{11} mode and (f) LSM^x_{01} mode.

However, the total loss of an SINRD waveguide is generally higher than that of its SIDW counterpart because of its metallic coatings or plates involved in its formation and more confined field pattern within the lossy dielectric material. SINRD-based architecture generally suffers from a relatively high conductor loss. Interestingly, it can be anticipated that a straightforward solution of hybrid waveguides in Fig. 1(b) should be attractive, which is set to combine the merits of each of those waveguides in a waveguide architecture [22]. This hybridization presents a reasonable compromise of transmission loss and circuit design through blending those DW variants altogether.

The key of the hybrid waveguide architecture is an effective transmission over the interface between SIDW and SINRD in Fig. 1(b). In this work, the feasibility of the proposed hybrid waveguide architecture is validated by studying the mode compatibility between the E^x_{11} mode of SIDW and the nonradiative LSM^x_{01} mode of SINRD waveguide. Then, this work devises and presents a straight back-to-back substrate-integrated hybrid metallo-dielectric (SIHMD) waveguide architecture composed of SIDW and SINRD waveguides.

II. Feasibility of Substrate-Integrated Hybrid MD Waveguide

A. SIDW and SINRD Waveguide

A general SIDW topology is shown in Fig. 2(a). By metallizing the substrate surface as shown in Fig. 2(b), one can have an SINRD waveguide within a certain bandwidth. In this work, alumina substrate with relative permittivity of 9.8 and thickness of $h = 0.254$ mm is used for WR3-band demonstration. Its cross section should be appropriately considered and designed to confine the guided electromagnetic fields. The width of the guiding channel is initially set to $w = 0.3$ mm. Air-hole perforation is applied over the bilateral section next to the guiding channel to reduce the dielectric permittivity of the hosting substrate. Even though it resembles a photonic bandgap structure [23], [24], their nature of operation is completely different. In this work, equivalent models in Fig. 2(c) and (d) are used to characterize the SIDW and SINRD waveguide. In this way, the SIDW and SINRD are simplified as a composite guide consisting of an unperforated dielectric guiding channel of rectangular cross section and its surrounding materials with an air-perforation-induced lower equivalent homogeneous or effective permittivity. According to [1] and [14], the dispersion curves of SIDW and SINRD can be obtained. As shown in Fig. 3, both the SIDW and SINRD waveguides of interest are set to work in the WR3-band. The SIDW supports the fundamental E^x_{11} and E^y_{11} modes, whereas the SINRD supports the nonradiative LSE^x_{11} and LSM^x_{01} modes.

B. Substrate-Integrated Hybrid MD Waveguide

The feasibility of a hybrid waveguide architecture consisting of both waveguides can be evaluated in a straightforward manner. As discussed in [1], while cascading two different

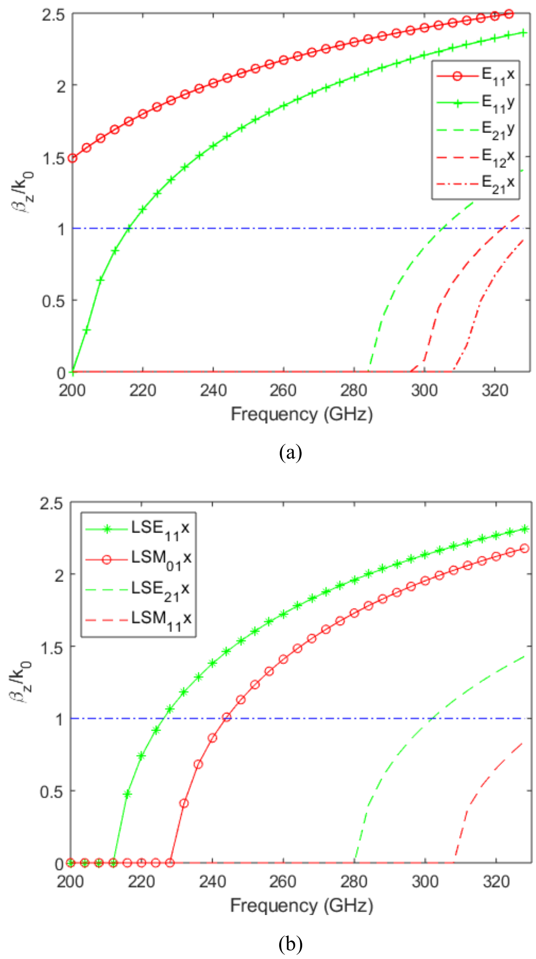

Fig. 3. Dispersion curves of (a) SIDW and (b) SINRD waveguide. Parameters: $h = 0.254$ mm, $w = 0.3$ mm, $\varepsilon_{r1} = 9.8$, and $\varepsilon_{r2} = 3$.

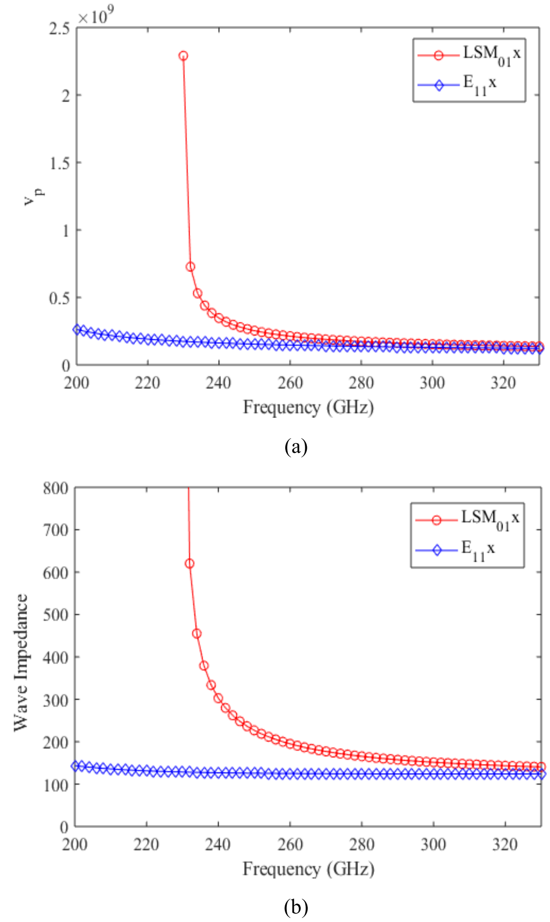

Fig. 4. (a) Phase velocities of SIDW and SINRD waveguide. (b) Wave impedances of SIDW and SINRD waveguide.

types of waveguides to achieve efficient power coupling and signal transmission, three conditions should generally be satisfied, namely, field matching, phase velocity matching, and impedance matching.

According to field equations (1) and (2) in the Appendix, one can figure out that the E_{11}^x mode of SIDW and the LSM_{01}^x mode of SINRD waveguide have similar transverse electric field patterns, as shown in Fig. 2(e) and (f). The phase velocities of the E_{11}^x mode and the LSM_{01}^x mode are plotted in Fig. 4(a), showing a good matching condition. According to (3) in the Appendix, the wave impedances of those two modes are also plotted in Fig. 4(b). In this case, they are found to converge toward each other as frequency increases, which indicates the possibility of a good impedance matching between the two waveguides.

The structure of the SIHMD waveguide architecture is shown in Fig. 5(a). The SIDW is directly connected to an SINRD waveguide without resorting to any geometrical adjustment and compensation. The simulated result is given in Fig. 5(b). As indicated, power or signal can be effectively coupled from the SIDW to the SINRD waveguide. The operating band starts from 260 GHz with a maximum loss of 0.3 dB. The bandwidth of the SIHMD waveguide architecture is mainly decided by that of the SINRD waveguide. As suggested in Fig. 3(b), the cutoff frequency of the LSM_{01}^x mode of the given SINRD waveguide is 230 GHz. The upper end of the SINRD waveguide is determined by the cutoff frequency of the first higher order parallel-plate waveguide (PPW) mode of the dielectric-loaded PPW. For the given SINRD waveguide, the first higher order PPW mode propagating in region #2 with $\varepsilon_{r2} = 3$ appears at 340 GHz [25]. Theoretically, the appearance of the higher order PPW mode can be moved backward by decreasing the effective permittivity of region #2. However, decreasing ε_{r2} by increasing the density of air holes would adversely fragilize the structure.

The average insertion loss of the proposed SIHMD waveguide architecture, mainly caused by impedance mismatch, is about 0.15 dB over the bandwidth from 260 to 330 GHz. Both the phase velocity and the wave impedance of the E_{11}^x mode converge with those of the LSM_{01}^x mode as frequency increases, which results in a better impedance match. The field distribution of the SIHMD waveguide architecture is plotted in Fig. 5(c) and (d).

III. Back-to-Back SIHMD Waveguide

A. Proposed SIHMD Waveguide Architecture Consisting of SIDW and SINRD

A back-to-back SIHMD waveguide architecture consisting of SIDW and SINRD for the WR3-band is demonstrated. Its layout is sketched in Fig. 6(a). An alumina substrate with a

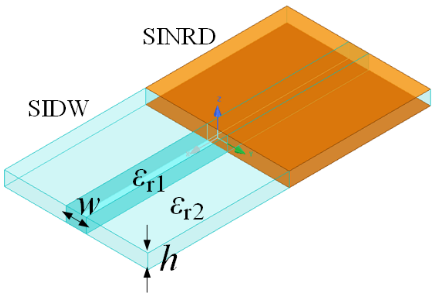

(a)

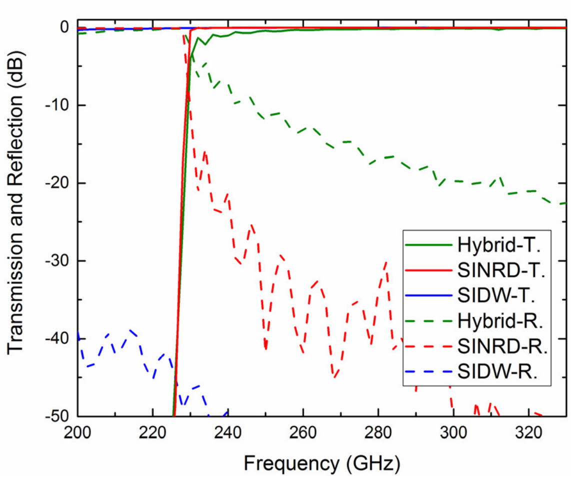

(b)

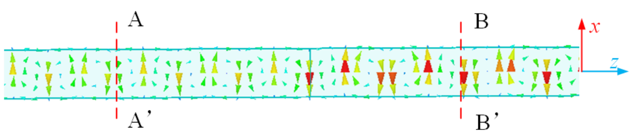

(c)

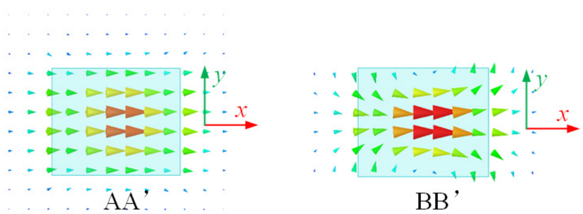

(d)

Fig. 5. (a) Equivalent model of SIHMD waveguide. (b) Transmissions and reflections of SIDW, SINRD, and SIHMD structures. (c) Electric field distributions of SIHMD waveguide architecture at the xoz plane. (d) E^x_{11} mode at AA' (left) and LSM^x_{01} mode at BB' (right). Parameters: $h = 0.254$ mm, $w = 0.3$ mm, $\varepsilon_{r1} = 9.8$, and $\varepsilon_{r2} = 3$.

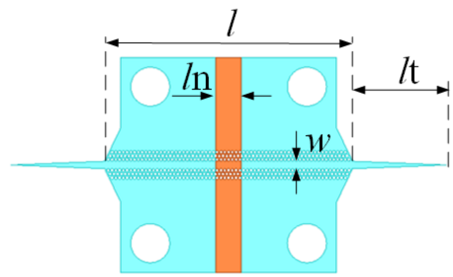

(a)

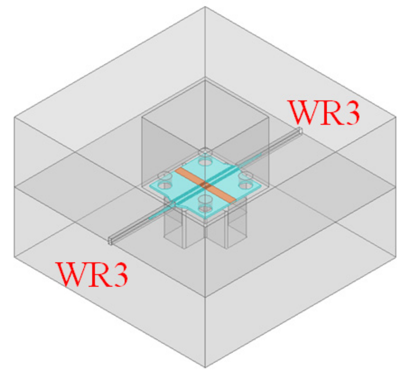

(b)

Fig. 6. (a) Layout of the proposed back-to-back SIHMD waveguide architecture. (b) Metallic housing used to support the waveguide under testing. Parameters: $l = 10$ mm, $w = 0.3$ mm, $l_t = 3.5$ mm, and $l_n = 1.75$ mm. More details can be found in Table I.

thickness of $h = 0.254$ mm is used to develop the SIHMD waveguide architecture prototype with a length of $l = 10$ mm and a width of $w = 0.3$ mm. In this work, a fabricated prototype with the SINRD waveguide length of $l_n = 1.75$ mm is demonstrated and experimentally verified.

The periodicity of air hole perforation $p = 0.15$ mm considered here is smaller than the operating guided wavelength to avoid the electromagnetic band gap in the band of interest. The diameter of the air hole is set as $d = 0.125$ mm. The wall thickness between two adjacent air holes is $a = g = 0.025$ mm, reaching the manufacturing limit of our laser drilling system in the Poly-Grames Research Center. Approximate values of the permittivity of the given perforated substrate are around $\varepsilon_{r2x} = \varepsilon_{r2z} = 3.2$ for the horizontal polarization and $\varepsilon_{r2y} = 4.25$ for the vertical polarization by using the characteristic equations formulated and examined in [26]. The same air-hole perforation pattern is used throughout the SIHMD waveguide architecture.

The loss tangent of the alumina substrate is about tan $\delta = 0.001$ in simulation. The conductivity of the gold metallic coatings is set to $\sigma = 4.1 \times 10^7$ S/m in our HFSS simulations without considering potential surface roughness. A metallic housing is required for the measurement of the SIHMD waveguide, as shown in Fig. 6(b). To maintain the field pattern of the SIDW, the metal is removed underneath and above the SIDW sections. The substrate is bilaterally extended and suspended within the metallic housing. The SIHMD waveguide is tapered with a length of $l_t = 3.5$ mm at both ends for impedance matching between the air-filled standard rectangular waveguide and the SIDW. The standard WR3-band rectangular waveguides (0.8636 mm $\times$ 0.4318 mm) are rotated to excite the horizontally polarized modes. The electromagnetic wave can successfully propagate through the SIDW-SINRD-SIDW architecture in Fig. 7.

The fabricated prototype of the demonstrated SIHMD waveguide architecture is shown in Fig. 8. Air-hole perforation was performed by laser micromachining. The taper length is $l_t = 3.35$ mm, a value smaller than the designed counterpart

TABLE I
PARAMETERS OF DEMONSTRATED SIHMD WAVEGUIDE ARCHITECTURE

Symbol	Description	Quantity
w	width of guiding core	0.3 mm
h	thickness of hosting substrate	0.254 mm
d	diameter of air hole	0.125 mm
a/g	thickness of wall between adjacent holes	0.025 mm
ε_{r1}	relative permittivity of the hosting substrate	9.8
ε_{r2}	effective relative permittivity in region #2 used in equivalent models	3
l	total length of the demonstrated SIHMD	10 mm
l_t	length of the taper for matching	3.5 mm
l_n	length of SINRD waveguide	1.75 mm
σ	conductivity of gold in simulation	4.1×10^7 S/m
tan δ	loss tangent of alumina in simulation	0.001

The dimension of WR3-band rectangular waveguide used in simulation is 0.8636 mm×0.4318 mm.

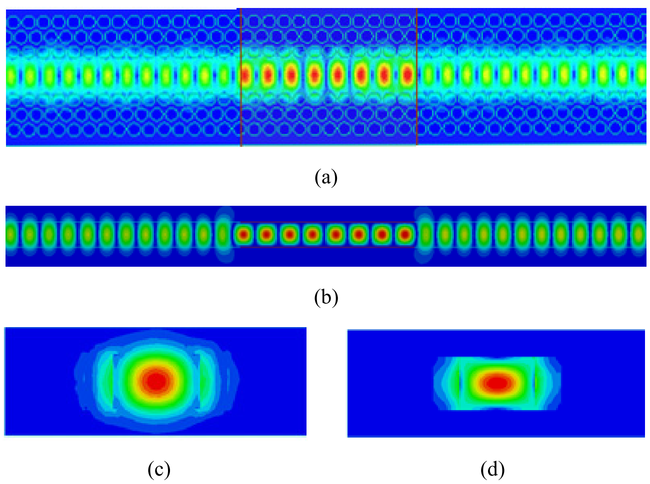

Fig. 7. Simulated electric field distributions of the proposed back-to-back SIHMD waveguide architecture at 280 GHz. (a) Top view, (b) side view, (c) cross section of SIDW, E_{11}^x mode, and (d) cross section of SINRD waveguide, LSM_{01}^x mode.

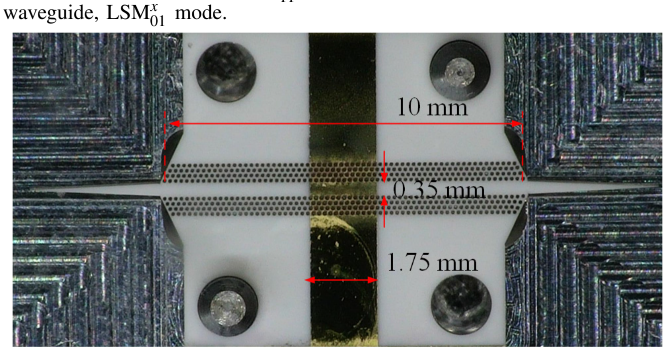

Fig. 8. Photograph of the presented back-to-back SIHMD waveguide architecture under microscope.

since the tip has been burned during the manufacturing process. The metallic coatings were obtained by standard lithography before the air-hole perforation to avoid unwanted metal deposition into air holes.

S-parameters were measured using a PNA-X with VDI frequency extenders. Thru-reflect-line calibration was performed up to the edges of the metallic support. Fig. 9 shows the comparison between the measured results (solid lines) and full-wave simulation results (dashed lines). The average insertion loss is around 2.4 dB, which shows a good agreement with the simulated result (2.2 dB).

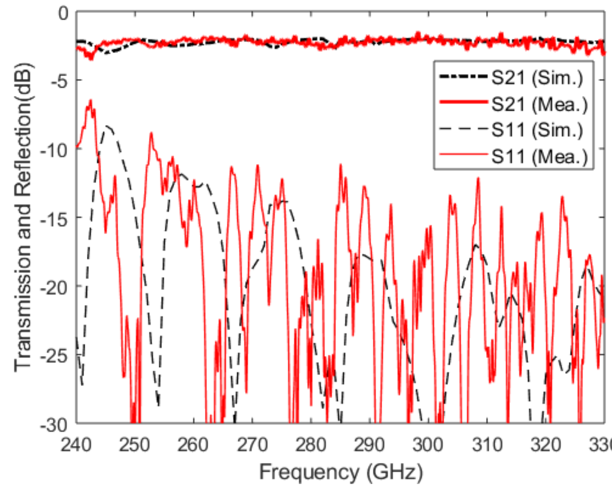

Fig. 9. Simulated and measured results of the presented back-to-back SIHMD waveguide architecture.

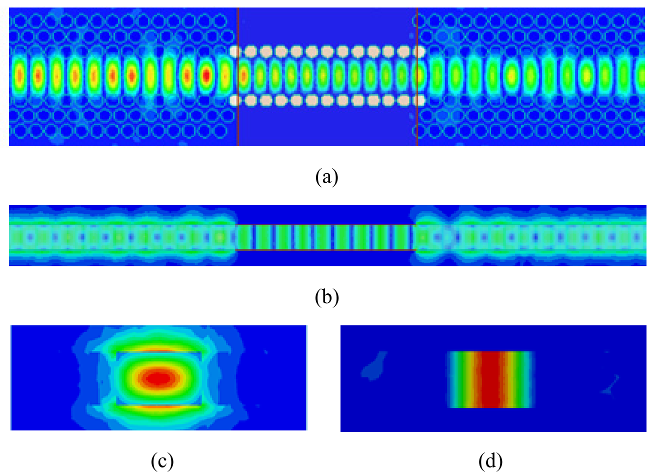

Fig. 10. Simulated electric field distributions of the traditional back-to-back SIHMD waveguide architecture (SIDW and SIW) at 280 GHz. (a) Top view, (b) side view, (c) cross section of the SIDW, E_{11}^y mode, and (d) cross section of the SIW waveguide, TE_{10}^z mode.

B. Comparison With SIHMD Waveguide Architecture Consisting of SIDW and SIW

As mentioned earlier, the traditional SIHMD waveguide architecture consists of SIW, which is also capable of confining electromagnetic waves at discontinuities. A comparison between the two SIHMD waveguide architectures is given here. The length of the SIW is selected to be the same as the SINRD waveguide in the proposed SIHMD scheme. No transition is added between two involved waveguides for each hybrid waveguide architecture. The coupling efficiency between the SIDW and SIW can be guaranteed because of the mode compatibility between the E_{11}^y/E_{11}^x mode and the $\mathrm{TE}_{10}^z/\mathrm{TE}_{01}^z$ mode if the SIW has two continuous metallized walls. For the given SIDW-SIW-SIDW in Fig. 10, the operating mode is the E_{11}^y mode in SIDW and the TE_{10}^z mode in SIW with two rows of metallized via holes. Simulated electric field distribution is carried out by using of HFSS

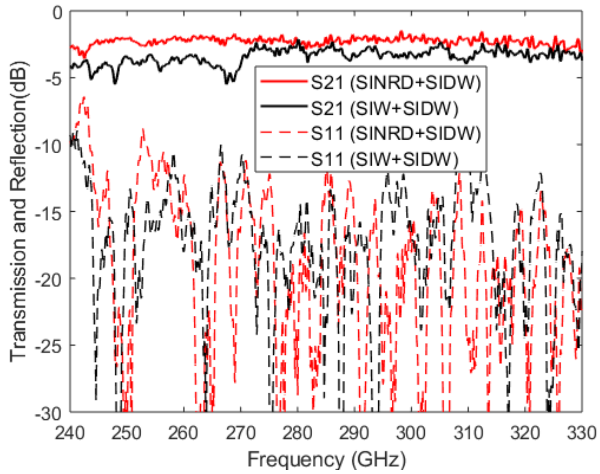

Fig. 11. Comparison between the measured S-parameters of two SIHMD waveguide architectures.

package. Obviously, the electromagnetic wave can successfully propagate through the SIDW-SIW-SIDW architecture. Metallic housing similar to that in Fig. 6(b) but with differently oriented transitions is fabricated to measure the back-to-back SIDW-SIW-SIDW architecture. The measured results are plotted in Fig. 11.

The transmission coefficient of the proposed SIHMD waveguide architecture is 1 dB better on average. Comparing the SIHMD of SIDW and SIW, where the manufacturing process of metallized via holes could introduce more fabrication complexity, the presented SIHMD of SIDW and SINRD is preferred with its superior performance. Note that the mode operating in SIDW of the proposed SIHMD waveguide architecture is the E_{11}^x mode to ensure that the excited mode in SINRD is the nonradiative LSM_{01}^x mode. Otherwise, the E_{11}^y mode in SIDW could excite the TE_{10}^z mode of the SINRD, which actually works as an H-guide [27], [28]. Again, additional measures are required to confine electromagnetic waves over the discontinuities since H-guide does not have this feature, leading to design complexity.

IV. Discussion

A parametric study based on HFSS simulations is given in this section to examine the influence of geometrical and substrate parameters on transmission properties of the proposed waveguide architecture. The SINRD waveguide and the SIDW are set to share the same width, which simplifies our analysis. The equivalent model used in this investigation is shown in Fig. 12(a).

A. Core Width

The frequency response of the SIHMD waveguide architecture with different waveguide widths is shown in Fig. 12(b). The operating band is downshifted after increasing the waveguide width. Also, the transmission coefficient increases with increasing waveguide width, as shown in Fig. 12(c), however, at the expense of a narrower bandwidth, as shown in Fig. 13(a).

B. Effective Permittivity of Perforated Region

In consideration of the structural feasibility of SINRD waveguide, the diameter of air holes has been reduced to

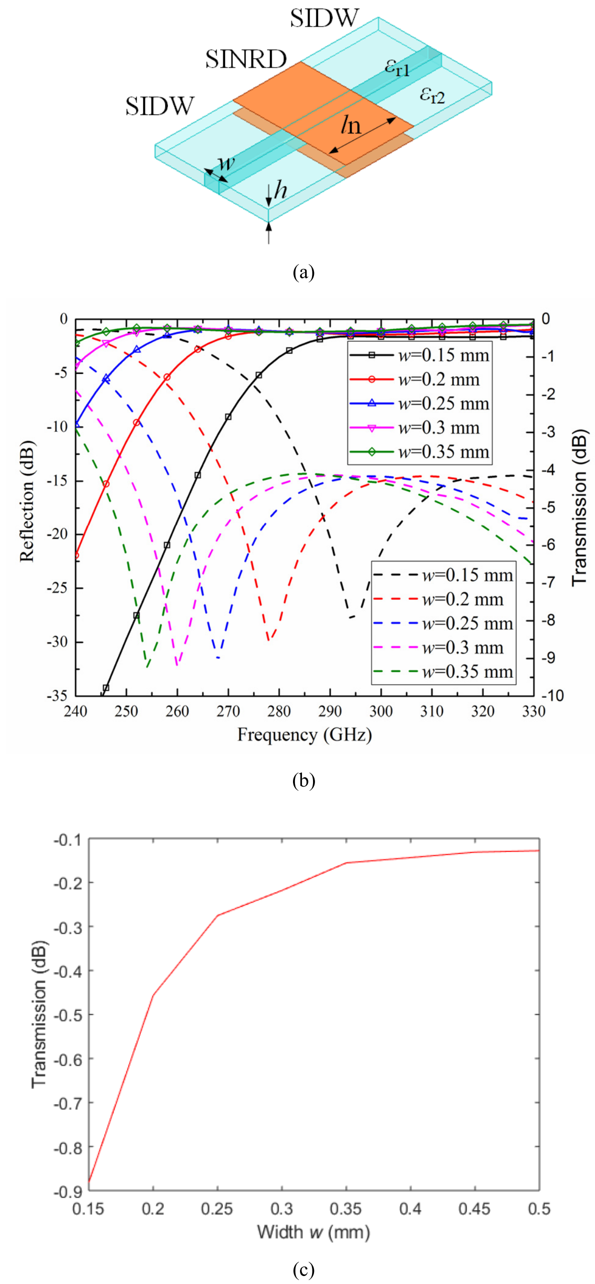

Fig. 12. (a) Equivalent model of the proposed back-to-back SIHMD waveguide architecture. (b) Transmissions and reflections of the back-to-back SIHMD waveguide architecture with different SINRD widths. (c) Transmission of the back-to-back SIHMD waveguide architecture with different widths at 330 GHz. Parameters: $h = 0.254$ mm, $w = 0.3$ mm, $l_n = 0.254$ mm, $\varepsilon_{r1} = 9.8$, and $\varepsilon_{r2} = 3$.

0.1 mm during fabrication, leading to a value of ε_{r2} larger than the expected one. Increasing ε_{r2} will push the related higher order PPW TE_1 mode into the band of interest, leading to a narrow nonradiative bandwidth. In practical applications, the bandwidth of LSM_{01}^x mode is terminated by either the higher order LSE_{21}^x mode or the PPW mode, whichever appears first. As shown in Fig. 13(b), ε_{r2} hardly affects the bandwidth of the LSM_{01}^x mode.

C. SINRD Waveguide

It is necessary to point out the effect of SINRD waveguide parameters, namely, the length and the roughness in our case,

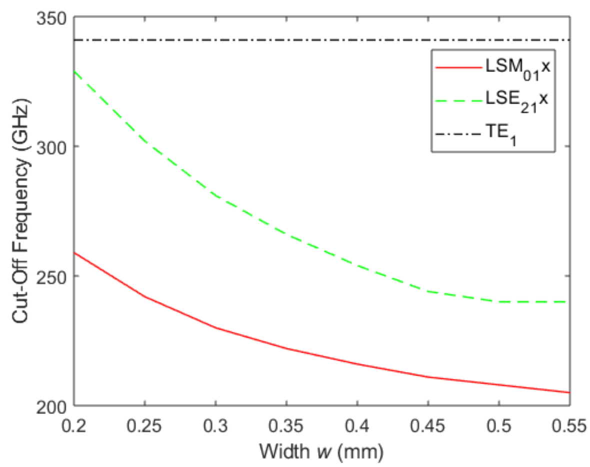

(a)

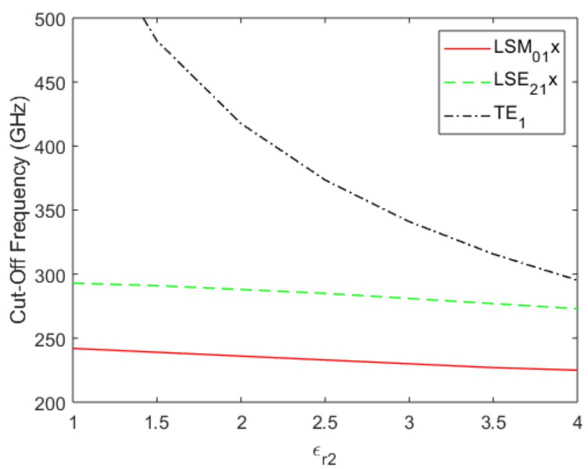

(b)

Fig. 13. (a) Width effect and (b) ε_{r2} effect on frequency response.

on the performance of the hybrid waveguide architecture. As shown in Fig. 14(a), the length of the SINRD waveguide section hardly affects the transmission performance as long as the material losses are excluded.

One needs to carefully decide the extent of the SINRD waveguide section since it could affect the overall loss performance of the proposed SIHMD waveguide architecture. The loss performance of both waveguides with the same dimensions and materials is analytically calculated based on their field distributions [1], [14] and the datasheet of given materials. It suggests that the SINRD waveguide has a higher loss (in turn SIHMD waveguide architecture), as shown in Fig. 14(b). First, the SINRD waveguide is not a conductor-loss-free structure because of the finite conductivity of metallic coatings. In addition, the SINRD waveguide typically has a higher dielectric loss because its field is more concentrated within the lossy dielectric core. As shown in Fig. 2(e) and (f), the field extends slightly to region #3 for the SIDW, whereas the field is completely confined between the two metallic coatings for the SINRD waveguide. Therefore, one should balance the system performance for specific scenarios. For example, while the space is not limited, smooth transition is allowed and SIDW is preferred. While discontinuities are densely distributed, involving SINRD waveguide can dramatically reduce the propagation path and, thus, the associated transmission loss.

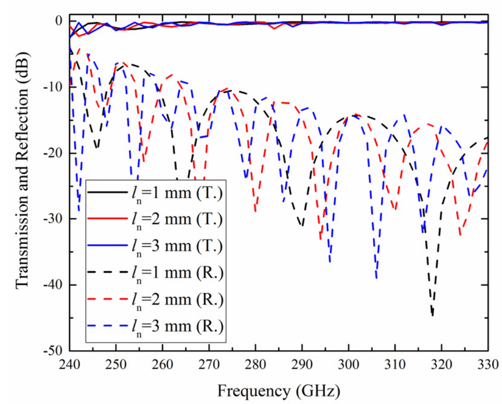

(a)

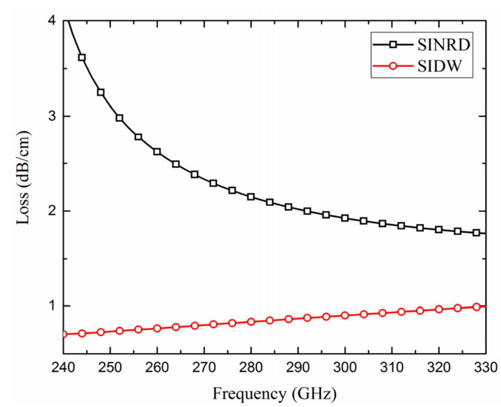

(b)

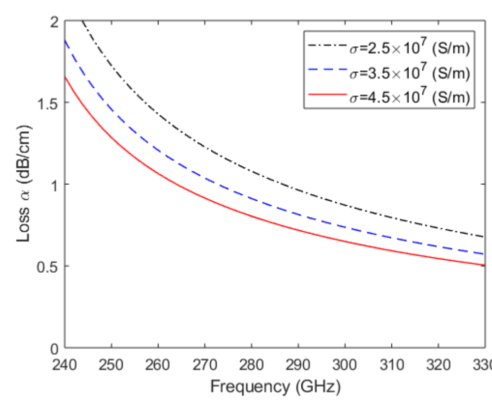

(c)

Fig. 14. (a) Transmissions and reflection of SIHMD waveguide architectures with different SINRD lengths ($w = 0.3$ mm). (b) Loss comparison between the SIDW and the SINRD waveguide. (c) Conductivity effect on the conductor loss of SINRD waveguide.

Next, the conductivity effect is examined on the transmission performance of SINRD waveguide. According to Fig. 14(c), reducing the conductivity slightly reduces the conductor loss. This phenomenon can be explained as follows. The dominant electric field component of the LSM_{01}^{x} mode is parallel to the two parallel metal coatings and is essentially close to zero near the metal coatings because of boundary conditions. Therefore, the transmission performance of the

SINRD waveguide is not that sensitive to surface roughness while operating in the LSM_{01}^{x} mode.

V. Conclusion

This work presents a hybrid waveguide architecture consisting of the SIDW and the SINRD waveguide, namely, the SIHMD waveguide architecture. The presented SIHMD waveguide architecture has been analyzed by full-wave simulations and experimentally verified in the WR3-band. The simulated average insertion loss is 2.2 dB for a back-to-back experimental prototype involving material losses, feeding loss, and reflection loss. The loss caused by the two interfaces between the SIDW and the SINRD waveguide is average 0.3 dB in total, as observed from the simulated transmission coefficient of the back-to-back SIHMD waveguide architecture. The proposed scheme shows a great potential in future mmW and THz applications.

Appendix

The dominant transverse field of the E_{11}^{x} mode of SIDW is given by

$$E_x = \begin{cases} A_1 \frac{(k_1^2-\beta_{x1}^2)}{j\omega\mu\varepsilon_1}\cos(\beta_{x1}x)\sin(\beta_{y1}y)e^{-j\beta_z z}, & \text{region \# 1} \\ A_2 \frac{(k_1^2+\beta_{x2}^2)}{j\omega\mu\varepsilon_2} e^{-\beta_{x2}x}e^{-\beta_{y2}y}e^{-j\beta_z z}, & \text{region \# 2} \\ A_3 \frac{(k_1^2+\beta_{x3}^2)}{j\omega\mu\varepsilon_3} e^{-\beta_{x3}x}e^{-\beta_{y3}y}e^{-j\beta_z z}, & \text{region \# 3.} \end{cases} \tag{1}$$

For the LSM_{01}^{x} mode of SINRD waveguide, the dominant transverse field is given by [14]

$$E_x = \begin{cases} B_1 \frac{(k_1^2-\beta_{x1}^2)}{j\omega\mu\varepsilon_1}\cos(\beta_{x1}x)\sin(\beta_y y)e^{-j\beta_z z}, & \text{region \# 1} \\ B_2 \frac{(k_1^2+\beta_{x2}^2)}{j\omega\mu\varepsilon_2} e^{-\beta_{x2}x}\sin(\beta_y y)e^{-j\beta_z z}, & \text{region \# 2} \end{cases} \tag{2}$$

where c and ω are, respectively, the free-space speed of light and radian frequency, k_1 is the propagation constant in region #1 in Fig. 2(c) and (d), w and h are, respectively, the width and the height of the SIDW core, m and n are the orders of modes, and ε_{r1}, ε_{r2}, and ε_{r3} are, respectively, the relative permittivity of regions #1, #2, and #3. $\beta_{x/y,1/2/3}$ is the propagation constant along the x-/y-axis at region #1/2/3. β_z is the propagation constant along the z-direction. $\mathrm{A/B}_{1,2,3}$ is the amplitude of electric fields for the corresponding mode at regions #1, #2, and #3.

For the SIDW operating in the E_{11}^{x} mode and the SINRD waveguide operating in the LSM_{01}^{x} mode, the wave impedance is given by

$$Z_w = \frac{E_t}{H_t} = \frac{k_1^2-\beta_{x1}^2}{\omega\varepsilon_1\beta_z}. \tag{3}$$

Acknowledgment

The authors would like to thank Traian Antonescu and Steve Dubé, with the fabrication of the structures, and Pascal Burasa for his assistance with measurements. All three are with the Poly-Grames Research Center at Polytechnique Montréal.

References

[1] C. Yeh and F. I. Shimabukuro, *The Essence of Dielectric Waveguides*. New York, NY, USA: Springer, 2008.

[2] E. A. J. Marcatili, “Dielectric rectangular waveguide and directional couplers for integrated optics,” *Bell Syst. Tech. J.*, vol. 48, no. 7, pp. 2071–2102, Sep. 1969.

[3] A. Malekabadi, S. A. Charlebois, D. Deslandes, and F. Boone, “High-resistivity silicon dielectric ribbon waveguide for single-mode low-loss propagation at F/G-bands,” *IEEE Trans. Terahertz Sci. Technol.*, vol. 4, no. 4, pp. 447–453, Jul. 2014.

[4] H.-T. Zhu et al., “Low-loss, thermally insulating, and flexible rectangular dielectric waveguide for sub-THz—Signal coupling in superconducting receivers,” *IEEE Trans. Terahertz Sci. Technol.*, vol. 10, no. 2, pp. 190–199, Mar. 2020.

[5] B. Yu, Y. Liu, Y. Ye, J. Ren, X. Liu, and Q. J. Gu, “High-efficiency micromachined sub-THz channels for low-cost interconnect for planar integrated circuits,” *IEEE Trans. Microw. Theory Techn.*, vol. 64, no. 1, pp. 96–105, Jan. 2016.

[6] N. Ranjkesh, M. Basha, A. Taeb, and S. Safavi-Naeini, “Silicon-on-glass dielectric waveguide—Part II: For THz applications,” *IEEE Trans. Terahertz Sci. Technol.*, vol. 5, no. 2, pp. 280–287, Mar. 2015.

[7] H. Amarloo, N. Ranjkesh, and S. Safavi-Naeini, “Terahertz silicon–BCB–quartz dielectric waveguide: An efficient platform for compact THz systems,” *IEEE Trans. Terahertz Sci. Technol.*, vol. 8, no. 2, pp. 201–208, Mar. 2018.

[8] C. Yeh, F. I. Shimabukuro, and J. Chu, “Dielectric ribbon waveguide: An optimum configuration for ultra-low-loss millimeter/submillimeter dielectric waveguide,” *IEEE Trans. Microw. Theory Techn.*, vol. 38, no. 6, pp. 691–702. Jan. 1990.

[9] C. Yeh, F. Shimabukuro, P. Stanton, V. Jamnejad, W. Imbriale, and F. Manshadi, “Communication at millimetre–submillimetre wavelengths using a ceramic ribbon,” *Nature*, vol. 404, no. 6778, pp. 584–588, Apr. 2000.

[10] C. Yeh, F. Shimabukuro, and P. H. Siegel, “Low-loss terahertz ribbon waveguides,” *Appl. Opt.*, vol. 44, no. 28, pp. 5937–5946, Oct. 2005.

[11] W. Gao et al., “Characteristics of effective-medium-clad dielectric waveguides,” *IEEE Trans. Terahertz Sci. Technol.*, vol. 11, no. 1, pp. 28–41, Jan. 2021.

[12] A. Patrovsky and K. Wu, “Substrate integrated image guide (SIIG)—A planar dielectric waveguide technology for millimeter-wave applications,” *IEEE Trans. Microw. Theory Techn.*, vol. 54, no. 6, pp. 2872–2879, Jun. 2006.

[13] D. C. Lugo, J. Wang, and T. M. Weller, “Analytical and experimental study of multilayer dielectric rod waveguides,” *IEEE Trans. Microw. Theory Techn.*, vol. 69, no. 4, pp. 2088–2097, Apr. 2021.

[14] T. Yoneyama and S. Nishida, “Nonradiative dielectric waveguide for millimeter-wave integrated circuits,” *IEEE Trans. Microw. Theory Techn.*, vol. MTT-29, no. 11, pp. 1188–1192, Nov. 1981.

[15] T. Yoneyama, M. Yamaguchi, and S. Nishida, “Coupling characteristics of nonradiative dielectric waveguides,” *IEEE Trans. Microw. Theory Techn.*, vol. MTT-31, no. 8, pp. 648–654, Aug. 1983.

[16] T. Yoneyama, M. Yamaguchi, and S. Nishida, “Bends in nonradiative dielectric waveguides,” *IEEE Trans. Microw. Theory Techn.*, vol. MTT-30, no. 12, pp. 2146–2150, Dec. 1982.

[17] T. Yoneyama, H. Tamaki, and S. Nishida, “Analysis and measurements of nonradiative dielectric waveguide bends,” *IEEE Trans. Microw. Theory Techn.*, vol. MTT-34, no. 8, pp. 876–882, Aug. 1986.

[18] Y. Cassivi and K. Wu, “Substrate integrated nonradiative dielectric waveguide,” *IEEE Microw. Wireless Compon. Lett.*, vol. 14, no. 3, pp. 89–91, Mar. 2004.

[19] F. Xu and K. Wu, “Substrate integrated nonradiative dielectric waveguide structures directly fabricated on printed circuit boards and metallized dielectric layers,” *IEEE Trans. Microw. Theory Techn.*, vol. 59, no. 12, pp. 3076–3086, Dec. 2011.

[20] P. Mondal and K. Wu, “Single mode operation of substrate integrated non-radiative dielectric waveguide and an excitation scheme of LSE_{11} mode,” *IEEE Microw. Wireless Compon. Lett.*, vol. 23, no. 8, pp. 418–420, Aug. 2013.

[21] J. Dallaire and K. Wu, “Complete characterization of transmission losses in generalized nonradiative dielectric (NRD) waveguide,” *IEEE Trans. Microw. Theory Techn.*, vol. 48, no. 1, pp. 121–125, Jan. 2000.

[22] C. Liu and K. Wu, “Substrate-integrated hybrid metallo-dielectric waveguide for millimeter-wave and terahertz applications,” in *IEEE MTT-S Int. Microw. Symp. Dig.*, Jun. 2022, pp. 359–362.

[23] K. Tsuruda, M. Fujita, and T. Nagatsuma, “Extremely low-loss terahertz waveguide based on silicon photonic-crystal slab,” *Opt. Exp.*, vol. 23, no. 25, p. 31977, Dec. 2015.

[24] H. Mosallaei and Y. Rahmat-Samii, “Photonic band-gap (PBG) versus effective refractive index: A case study of dielectric nanocavities,” in *Proc. IEEE Antennas Propag. Soc. Int. Symp. Transmitting Waves Prog. Next Millennium. Dig. Held Conjunct, USNC/URSI Nat. Radio Sci. Meeting*, Aug. 2000, pp. 338–341.

[25] D. M. Pozar, *Microwave Engineering*. 4th ed. Hoboken, NJ, USA: Wiley, 2011.

[26] A. V. Subashiev and S. Luryi, “Modal control in semiconductor optical waveguides with uniaxially patterned layers,” *J. Lightw. Technol.*, vol. 24, no. 3, pp. 1513–1522, Mar. 1, 2006.

[27] F. Tischer, “Properties of the H-guide at microwaves and millimeter waves,” in *Proc. WESCON Conf. Rec.*, 1958, pp. 4–12.

[28] C. Di Nallo, F. Frezza, A. Galli, P. Lampariello, and A. A. Oliner, “Properties of NRD-guide and H-guide higher-order modes: Physical and nonphysical ranges,” *IEEE Trans. Microw. Theory Techn.*, vol. 42, no. 12, pp. 2429–2434, Dec. 1994.

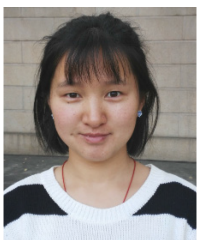

Chun-Mei Liu (Graduate Student Member, IEEE) received the bachelor’s degree in electronic information science and technology from Southwest Petroleum University, Chengdu, China, in 2010, and the Ph.D. degree in radio physics from the University of Electronic Science and Technology of China (UESTC), Chengdu, in 2022. She is currently pursuing the Ph.D. degree at Polytechnique Montréal, Montreal, QC, Canada.

Her research interests include nonradiative dielectric waveguides, low-loss terahertz (THz) circuits, integrated systems, phased array antennas, MIMO, and ultrawideband antennas, and cavity antennas.

Louis-Philippe Carignan (Member, IEEE) received the Ph.D. degree from the Engineering Physics and the Electrical Engineering Departments, École Polytechnique de Montréal, Montréal, Montreal, QC, Canada, in 2012.

In June 2012, he joined the Research and Development Department, Apollo Microwaves Ltd., Dorval, QC, Canada. He worked as a Research Associate at the Poly-Grames Research Center, Polytechnique Montréal, Montreal, from 2019 to 2022. He joined the National Research Council of Canada in December 2022. His research interests include gyrotropic components, passive microwave components, very high-power components, reflectarrays, nanostructured magnetic materials, machine learning, and optical coherence tomography.

Shaoqiu Xiao (Member, IEEE) received the Ph.D. degree in electromagnetic field and microwave technology from the University of Electronic Science and Technology of China (UESTC), Chengdu, China, in 2003.

From January 2004 to June 2004, he joined UESTC, as an Assistant Professor. From July 2004 to March 2006, he worked with the Wireless Communications Laboratory, National Institute of Information and Communications Technology of Japan (NICT), Singapore, as a Research Fellow, with a focus on the planar antenna and smart antenna design and optimization. From July 2006 to June 2010, he worked with the UESTC, as an Associate Professor, and from August 2010 to December 2019, he worked for UESTC, as a Professor. He visited Ecole Normale Superieure de Cachan, Paris, France, as a Senior Research Scholar, from July 2015 to August 2015. In January 2020, he joined Sun Yat-sen University, Guangzhou, China, as a Professor. He has authored/coauthored more than 300 technical journals, conference papers, books, and book chapters. His current research interests include planar antenna and phased array, microwave passive circuits, and time reversal electromagnetics.

Yejun He (Senior Member, IEEE) received the Ph.D. degree in information and communication engineering from the Huazhong University of Science and Technology (HUST), Wuhan, China, in 2005.

From 2005 to 2006, he was a Research Associate with the Department of Electronic and Information Engineering, The Hong Kong Polytechnic University, Hong Kong. From 2006 to 2007, he was a Research Associate with the Department of Electronic Engineering, Faculty of Engineering, The Chinese University of Hong Kong, Hong Kong. In 2012, he was a Visiting Professor with the Department of Electrical and Computer Engineering, University of Waterloo, Waterloo, ON, Canada. From 2013 to 2015, he was an Advanced Visiting Scholar (Visiting Professor) with the School of Electrical and Computer Engineering, Georgia Institute of Technology, Atlanta, GA, USA. Since 2011, he has been a Full Professor with the College of Electronics and Information Engineering, Shenzhen University, Shenzhen, China, where he is the Director of the Guangdong Engineering Research Center of Base Station Antennas and Propagation, Shenzhen, and the Director of the Shenzhen Key Laboratory of Antennas and Propagation, Shenzhen. He was selected as Pengcheng Scholar Distinguished Professor, Shenzhen, and a Minjiang Scholar Chair Professor of Fujian, China, in 2020 and 2022, respectively. He has authored or coauthored over 260 research papers and seven books, and holds about 20 patents. His research interests include wireless communications, antennas, and radio frequency.

Dr. He is a Fellow of IET and a Senior Member of the China Institute of Communications and the China Institute of Electronics. He was a recipient of the Shenzhen Overseas High-Caliber Personnel Level B (“Peacock Plan Award” B) and Shenzhen High-Level Professional Talent (Local Leading Talent). He received the Shenzhen Science and Technology Progress Award in 2017 and the Guangdong Provincial Science and Technology Progress Award for two times in 2018 and 2023. He is currently the Chair of the IEEE Antennas and Propagation Society-Shenzhen Chapter and obtained the 2022 IEEE APS Outstanding Chapter Award. He has served as a Reviewer for various journals, such as the IEEE TRANSACTIONS ON VEHICULAR TECHNOLOGY, the IEEE TRANSACTIONS ON COMMUNICATIONS, the IEEE TRANSACTIONS ON INDUSTRIAL ELECTRONICS, the IEEE TRANSACTIONS ON ANTENNAS AND PROPAGATION, the IEEE WIRELESS COMMUNICATIONS, the IEEE COMMUNICATIONS LETTERS, the *International Journal of Communication Systems, Wireless Communications and Mobile Computing*, and *Wireless Personal Communications*. He has also served as a Technical Program Committee Member or a Session Chair for various conferences, including the IEEE Global Telecommunications Conference (GLOBECOM), the IEEE International Conference on Communications (ICC), the IEEE Wireless Communication Networking Conference (WCNC), APCAP, EUCAP, UCMMT, and the IEEE Vehicular Technology Conference (VTC). He served as the TPC Chair for IEEE ComComAp 2021, the General Chair for IEEE ComComAp 2019, the TPC Co-Chair for WOCC 2023/2022/2019/2015, and the Organizing Committee Vice Chair for the International Conference on Communications and Mobile Computing (CMC 2010). He acted as the Publicity Chair for several international conferences, such as the IEEE PIMRC 2012. He is the Principal Investigator for over 30 current or finished research projects, including the National Natural Science Foundation of China, the Science and Technology Program of Guangdong Province, and the Science and Technology Program of Shenzhen City. He is serving as an Associate Editor for IEEE TRANSACTIONS ON ANTENNAS AND PROPAGATION, IEEE TRANSACTIONS ON MOBILE COMPUTING, *IEEE Antennas and Propagation Magazine*, IEEE ANTENNAS AND WIRELESS PROPAGATION LETTERS, *International Journal of Communication Systems China Communications*, and *Wireless Communications and Mobile Computing*. He served as an Associate Editor for Security and Communication Networks journal and IEEE Network.

Ke Wu (Fellow, IEEE) received the B.Sc. degree (Hons.) in radio engineering from the Nanjing Institute of Technology (now Southeast University), Nanjing, China, in 1982, and the D.E.A. degree (Hons.) and Ph.D. degree (Hons.) in optics, optoelectronics, and microwave engineering from the Institut National Polytechnique de Grenoble (INPG), University of Grenoble, Grenoble, France.

He was the Founding Director of the Center for Radio frequency Electronics Research, Montreal, QC, Canada (Regroupement stratégique of FRQNT), and the Canada Research Chair of RF and Millimeter-Wave Engineering. He is currently a Professor of electrical engineering and the Industrial Research Chair in Future Wireless Technologies with the Polytechnique Montréal, Montreal, where he is also the Director of the Poly-Grames Research Center. He has authored or coauthored over 1400 referred articles and numerous books/book chapters, and filed over 80 patents. His current research interests involve substrate-integrated antennas/circuits/systems, antenna arrays, field theory and joint field/circuit modeling, ultrafast guided-wave electronics, wireless power transmission and harvesting, microwave photonics, and megahertz-through-terahertz (THz) technologies and transceivers, including radio-frequency integrated circuits (RFICs)/monolithic microwave integrated circuits (MMICs) for joint radar/communication architectures, innovative multifunction wireless systems, and biomedical applications.

Dr. Wu is a Fellow of the Canadian Academy of Engineering, the Academy of Science of the Royal Society of Canada, and the German National Academy of Science and Engineering (acatech). He is a member of the Electromagnetics Academy, URSI, and IEEE-Eta Kappa Nu (IEEE-HKN). He was a recipient of many awards and prizes, including the inaugural IEEE MTT-S Outstanding Young Engineer Award, the 2004 Fessenden Medal of the IEEE Canada, the 2009 Thomas W. Eadie Medal of the Royal Society of Canada, the Queen Elizabeth II Diamond Jubilee Medal in 2013, the 2013 FCCP Education Foundation Award of Merit, the 2014 IEEE MTT-S Microwave Application Award, the 2014 Marie-Victorin Prize (Prix du Quebec), the 2015 Prix d'Excellence en Recherche et Innovation of Polytechnique Montréal, the 2015 IEEE Montreal Section Gold Medal of Achievement, the 2019 IEEE MTT-S Microwave Prize, the 2021 EIC Julian C. Smith Medal, the 2022 IEEE MTT-S Outstanding Educator Award, and the 2022 IEEE AP-S John Kraus Antenna Award. He has held key positions in and has served on various panels and international committees, including the chair of technical program committees, international steering committees, and international conferences/symposia. In particular, he was the General Chair of the 2012 IEEE Microwave Theory and Techniques (IEEE MTT-S) and International Microwave Symposium (IMS) and the TPC Co-Chair of the 2020 IEEE International Symposium on Antennas and Propagation (APS). He was the Chair of the joint IEEE Montreal chapters of MTT-S/AP-S/LEOS and then the restructured IEEE MTT-S Montreal Chapter, Canada. He has served the IEEE MTT-S Administrative Committee (AdCom) as the Chair for the IEEE MTT-S Transnational Committee, the Member and Geographic Activities (MGA) Committee, Technical Coordinating Committee (TCC), and the 2016 IEEE MTT-S President among many other AdCom functions. He is currently the Chair of the IEEE MTT-S Inter-Society Committee. He was a Distinguished Microwave Lecturer of the IEEE MTT-S from 2009 to 2011. He served the European Microwave Association (EuMA) as the Inaugural Representative of North America in its General Assembly. He has served on the editorial/review boards for many technical journals, transactions, proceedings, and letters as well as scientific encyclopedia, including an editor, a track editor, and a guest editor.